Letter

Ab initio study of ultrafast charge dynamics in graphene

Q. Z. Li,[1] P. Elliott,[1] J. K. Dewhurst,[2] S. Sharma,[1] and S. Shallcross[1]
[1]*Max-Born-Institute for Nonlinear Optics and Short Pulse Spectroscopy, Max-Born Strasse 2A, 12489 Berlin, Germany*
[2]*Max-Planck-Institut fur Mikrostrukturphysik, Weinberg 2, D-06120 Halle, Germany*

(Received 2 December 2020; revised 13 January 2021; accepted 13 January 2021; published 5 February 2021)

Monolayer graphene provides an ideal material to explore one of the fundamental light-field driven interference effects: Landau-Zener-Stückelberg interference. However, direct observation of the resulting interference patterns in momentum space has not proven possible, with Landau-Zener-Stückelberg interference observed only indirectly through optically induced residual currents. Here we show that the transient electron momentum density (EMD), an object that can easily be obtained in experiment, provides an excellent description of momentum resolved charge excitation. We employ state-of-the-art time-dependent density function theory calculations, demonstrating by direct comparison of EMD with conduction band occupancy, obtained from projecting the time propagated wave function onto the ground state, that the two quantities are in excellent agreement. For even the most intense laser pulses we find the electron dynamics to be almost completely dominated by the π band, with transitions to other bands strongly suppressed. Simple model based tight-binding approaches can thus be expected to provide an excellent description for the laser induced electron dynamics in graphene.

DOI: 10.1103/PhysRevB.103.L081102

Intense laser light offers the possibility to control electrons in matter on femtosecond timescales. Triumphs of this burgeoning field include tuning the optically induced current in graphene via the carrier envelope phase of light [1–3], attosecond control over magnetic order in thin films of magnetic overlayers [4,5], and controlled valley excitation in the semiconducting few layer dichalcogenides by circularly polarized light [6,7] to name only a few examples. The two band Dirac cone found in graphene provides an ideal materials platform for studying one of the canonical light-field driven interference effects: Landau-Zener-Stückelberg (LZS) interference [8,9], which before its observation in graphene [3] had only been observed in designed two state quantum systems [10–14]. This effect occurs when an oscillating electromagnetic field drives intraband oscillation through the Bloch acceleration theorem $\mathbf{k} \rightarrow \mathbf{k} + \mathbf{A}(t)/c$ and in the region of an avoided crossing interband transitions occur even when the band gap exceeds the dominant pulse frequency, so-called Landau-Zener transitions. Upon repeated passing of the avoided crossing multiple pathways exist to the conduction band with consequent constructive and destructive interference of electron states. This offers rich possibilities for controlling electron dynamics by intense laser light, demonstrated by the recent observation of control over optical currents underpinned by LZS interference [3], a result anticipated theoretically in Ref. [15].

The ubiquity of the avoided crossing band structure in two-dimensional (2D) materials, found not only in the Dirac cone of graphene but also in the semiconducting monolayer dichalcogenides [16], phosphorene [17,18], silicene [19], and stanene [20], points towards the importance of LZS interferometry in controlling electron dynamics in 2D materials. However, while interference physics can be easily probed theoretically through the conduction band population [18,21,22], the experimental situation is more difficult, with to date only indirect observations of LZS physics in materials reported. In this Letter we show that the transient electron momentum density (EMD) difference, defined as

$$\Delta\rho(\mathbf{p}, t_f) = \rho(\mathbf{p}, t_f) - \rho(\mathbf{p}, t = 0) \tag{1}$$

with $\mathbf{p}$ momentum and $\rho(\mathbf{p}, t)$ the electron momentum density [23] before ($t = 0$) and after (t_f) the pump laser pulse, offers a tool for directly probing LZS interference effects. The EMD may be measured experimentally via tomographic reconstruction using Compton profiles [24–28] and, in particular, for layered materials [29,30]. Combining these techniques with ultrafast x-ray sources will allow the transient EMD to be experimentally measured. This suggests a way in which the LZS physics may be directly observed in 2D materials, opening the way to correlate indirect LZS physics such as induced currents with the fundamental momentum space interference patterns.

For graphene, we demonstrate that the EMD facilitates both the real time observation of the formation of LZS interference patterns, as well as the elucidation of subtle features in the relation between pump pulse and interference in momentum space.

In contrast to previous works that have employed simple single particle tight-binding Hamiltonians to study the LZS effect [3,18,21,22,31–34], we will here deploy the time-dependent version of density functional theory (TD-DFT). To establish the accuracy of the EMD as a record of LZS interference we compare it with the excited electron distribution, N_{ex}, defined within TD-DFT as [35]

$$N_{\mathrm{ex}}(\mathbf{k}, t) = \sum_{i}^{\mathrm{occ}} \sum_{j}^{\mathrm{unocc}} |\langle \psi_{i\mathbf{k}}(t) | \psi_{j\mathbf{k}}(t = 0) \rangle|^2, \tag{2}$$

where $\psi_{j\mathbf{k}}(t)$ is the time-dependent Kohn-Sham orbital at time t, and $\psi_{i\mathbf{k}}(t=0)$ is the ground-state orbital. In all cases we find that the pattern of excitation in momentum space generated by transient EMD and $N_{\rm ex}$ is nearly identical in the first Brillouin zone (BZ).

Finally, we consider the role of the non-π-band states in the electron dynamics in graphene. Remarkably, despite electron excitation through the whole energy range of the π band (up to 10 eV above the Fermi energy, an energy range encompassing the σ^* bands as well as several high l character bands), it turns out that there occur almost no transitions to states outside the π-band manifold. We attribute this to the near vanishing of the corresponding dipole matrix elements. Our calculations thus suggest that even for very significant laser excitation tight-binding based models will provide a good description of the electron dynamics.

According to the Runge-Gross theorem [36], which extends the Hohenberg-Kohn theorem into the time domain, with common initial states there will be a one to one correspondence between the time-dependent external potentials and densities [37,38]. Based on this theorem, a system of noninteracting particles can be chosen such that the density of this noninteracting system is equal to that of the interacting system for all times, with the wave function of this noninteracting system represented by a Slater determinant of single-particle orbitals. These time-dependent Kohn-Sham (KS) orbitals are governed by the Schrödinger equation (for the spin degenerate case):

$$i\partial_t \psi_j(\mathbf{r},t) = \left\{ \frac{1}{2}\left[-i\nabla + \frac{1}{c}\mathbf{A}_{\rm ext}(t) \right]^2 + v_s(\mathbf{r},t) \right\} \psi_j(\mathbf{r},t). \tag{3}$$

In the above equation $\mathbf{A}_{\rm ext}(t)$ is the vector potential representing the applied laser field, the effective potential $v_s(\mathbf{r},t)$ is given by $v_s(\mathbf{r},t) = v_{\rm ext}(\mathbf{r},t) + v_{\rm H}(\mathbf{r},t) + v_{\rm xc}(\mathbf{r},t)$, where $v_{\rm ext}(\mathbf{r},t)$ is the external potential, $v_{\rm H}(\mathbf{r},t)$ the Hartree potential, and $v_{\rm xc}(\mathbf{r},t)$ is the exchange-correlation (xc) potential. For the latter we have used the adiabatic local density approximation. From the Fourier transform of the Kohn-Sham states, $\psi_{i\mathbf{k}}(\mathbf{r})$, the electron momentum density can be constructed as $\rho(\mathbf{p}) = \sum_{i\mathbf{k}} |\psi_{i\mathbf{k}}(\mathbf{p})|^2$. This EMD constructed from KS states has been found to provide excellent agreement with that obtained from Compton scattering [23].

All calculations employ the state-of-the art all-electron full potential linearized augmented plane wave (LAPW) method [39], as implemented in the ELK code [40]. We have used a 30×30 **k**-point set; for further details of the implementation of TD-DFT within the LAPW basis we refer the reader to Refs. [41,42].

LZS interference probed by 2D tr-EMD. The patterns of excited charge in momentum space that most directly characterize Landau-Zener-Stückelberg interference are generally presented by plotting the conduction band occupation over the first Brillouin zone. However, this information, while easy to obtain theoretically, is difficult to obtain experimentally. We thus look at an alternative quantity; the change in electron momentum density due to the laser pulse.

In Fig. 1 are displayed the $N_{\rm ex}$, EMD, and induced currents for a diverse set of laser pulses exhibiting variation of several pulse parameters: carrier envelope phase (the angular difference between the **E** field and pulse envelope maxima), polarization, intensity, frequency, and full width half maximum (FWHM). The magnitude of the electric field is of the order of 5 V/nm, placing these pulses in the strong nonperturbative regime for graphene. As can be seen, in all cases

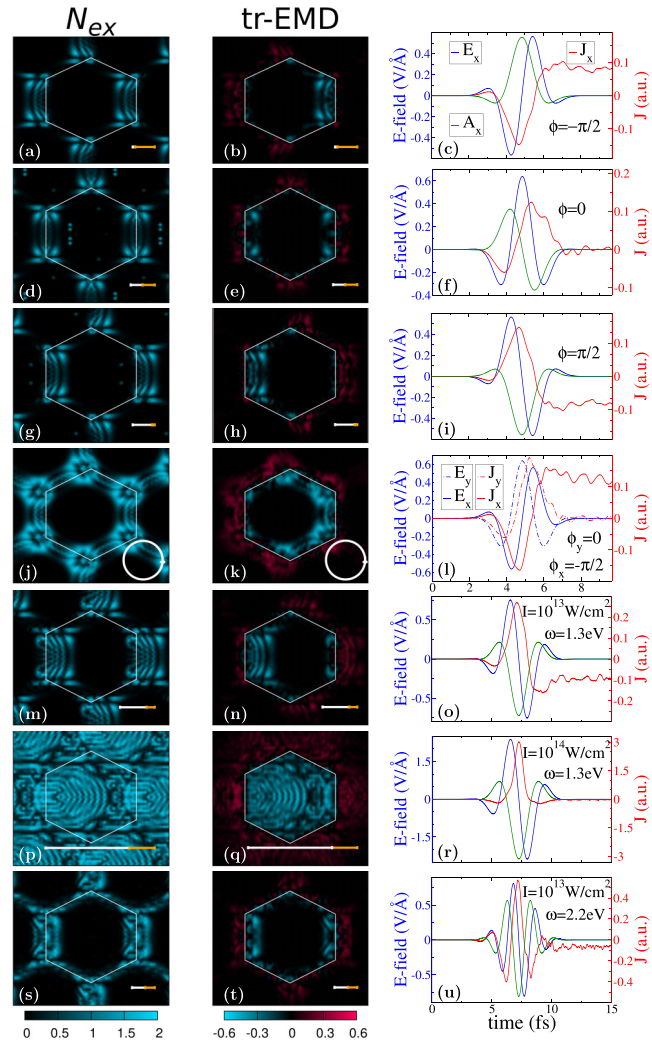

FIG. 1. Conduction band occupation as a function of **k** vector as determined directly by projection of the time-dependent state onto the ground-state Kohn-Sham states (first column) [see Eq. (2)] and, second column, the transient electron momentum density (tr-EMD) difference [see Eq. (1)]. Evidently, both quantities in a consistent way capture the momentum space intensity fringes generated by Landau-Zener-Stückelberg interference. The third column displays the electric field (**E** field) of the pump laser pulse (blue lines), the **A** field scaled such that it can be plotted on the same axis (green lines), and the induced current density (red lines). Pulses in (a)–(l) have a full width half maximum (FWHM) of 1.935 fs, a central frequency of 1.4 eV, and peak intensity of 5.43×10^{12} W/cm^2, and carrier envelope phase as indicated in the panels. The remaining three rows (m)–(u) have FWHM 2.758 fs, CEP of $\pi/2$, and central frequencies and intensities as indicated in the panels. In the first and second columns, the white hexagons represent the boundary of the first BZ while the lines in the right bottom corner represent the effective **k**-space trajectory given by the Bloch acceleration theorem.

$N_{\rm ex}$ and EMD convey consistent information concerning the excited charge, establishing the latter as a reliable probe of momentum space excitation.

Before exploring the LZS interference physics of graphene revealed in Fig. 1, we first provide a theoretical basis to this observed coincidence in the pattern of momentum space excitation between $N_{\rm ex}$ and EMD. The Kohn-Sham electron momentum density is defined as

$$\rho(\mathbf{p},t) = \sum_{j\mathbf{k}} f_{j\mathbf{k}} |\psi_{j\mathbf{k}}(\mathbf{p},t)|^2, \tag{4}$$

where

$$\psi_{j\mathbf{k}}(\mathbf{p},t) = \int d\mathbf{p}\, e^{i\mathbf{p}\cdot\mathbf{r}} \psi_{j\mathbf{k}}(\mathbf{r},t) \tag{5}$$

is the Fourier transform of the KS wave function $\psi_{j\mathbf{k}}$ and $f_{j\mathbf{k}}$ the occupation. Upon expansion of the Bloch functions in plane waves of the reciprocal lattice vectors, $\mathbf{G}$,

$$\psi_{j\mathbf{k}}(\mathbf{r},t) = \sum_{\mathbf{G}} c^{\mathbf{k}}_{j\mathbf{G}}(t) e^{i(\mathbf{k}+\mathbf{G})\cdot\mathbf{r}} \tag{6}$$

and insertion into Eqs. (4) and (5), we find that the EMD can be expressed as

$$\rho(\mathbf{p},t) = \sum_{j\mathbf{k}} f_{j\mathbf{k}} \sum_{\mathbf{G}} \left| c^{\mathbf{k}}_{j\mathbf{G}}(t) \right|^2 \delta(\mathbf{p}-\mathbf{k}-\mathbf{G}). \tag{7}$$

The EMD will therefore only change with respect to the ground-state EMD [see Eq. (1)] at points $\mathbf{p} = \mathbf{k} + \mathbf{G}$ where the coefficients $c^{\mathbf{k}}_{j\mathbf{G}}(t)$ change. In particular, in almost all systems, this will include the $\mathbf{G} = 0$ point, i.e., the $\mathbf{k}$ point itself within the first Brillouin zone. As the coefficient $c^{\mathbf{k}}_{j\mathbf{G}=0}(t_f)$ will change (w.r.t. the GS value) at points in k space where $N_{\rm ex}(\mathbf{k},t_f)$ is nonzero, $\Delta\rho(\mathbf{k},t_f)$ must also then be nonzero. Hence, any interference pattern seen in $N_{\rm ex}(\mathbf{k},t_f)$ will also be seen in $\Delta\rho(\mathbf{k},t_f)$. For two electron systems, it is known that the EMD produced from the KS wave function can differ significantly from the exact EMD [43,44]; however, in periodic systems, it was shown that the KS-EMD gives excellent agreement with Compton scattering profiles [23].

For a carrier envelope phase (CEP) of $\phi = \pm\pi/2$ the maximum **E**-field intensity, and hence the interband transition at the avoided crossing, occurs at the turning point of the path in momentum space executed due to the **A** field. As a result, the LZ transitions generate excited conduction band charge at either the positive ($\phi = +\pi/2$) or negative ($\phi = -\pi/2$) k_x sides of the Dirac point. This can be seen in rows (a)–(c) and (h)–(j) of Fig. 1. Note that positive and negative k_x, measured from the Dirac point, corresponds to the left- and right-hand sides of the vertical BZ boundary as seen in Fig. 1. In contrast, for $\phi = 0$ the maximum **E**-field intensity occurs at $\mathbf{A} = \mathbf{0}$ resulting in a symmetric excitation about the Dirac point [see rows (c)–(e)]. In the past such asymmetric LZS interference has been indirectly accessed by means of the net current that results from the asymmetric momentum space occupation for nonzero CEP, and to date this represents the only observation in experiment of LZS in a material [3]. This coherent current (current per unit cell) induced by the laser pulse is displayed in the third column of Figs. 1 and 2, and corresponds well with that seen in experiment. The experimentally accessible EMD,

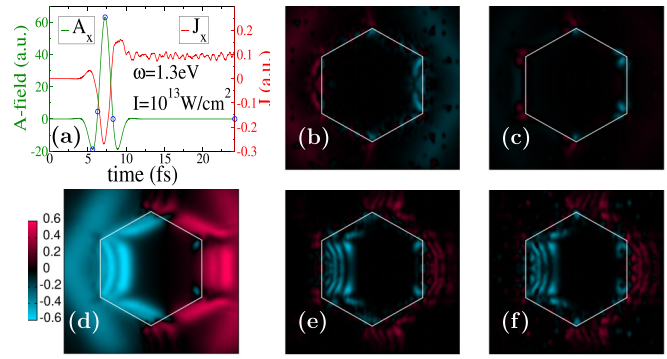

FIG. 2. Landau-Zener-Stückelberg interference in the first Brillouin zone (BZ) reflected by 2D transient electron momentum density (tr-EMD) at various time steps during and after the pulse. A pulse of central frequency 1.3 eV, intensity 1.0×10^{13} W/cm^2, full width half maximum 2.758 fs, and carrier envelope phase $\pi/2$ is employed, with the **A**-field exhibited and laser induced current exhibited in panel (a). The points on the **A**-field curve indicate the times at which the tr-EMD is evaluated, shown in panels (b)–(f). In these panels the full evolution of the Landau-Zener-Stückelberg (LZS) interference can be seen, including both early time $k_x < 0$ (left-hand side of the vertical BZ boundary line) conduction band excitation, intense excitation at the pulse peak, panel (d), before the development of the LZS interference fringes on the falling shoulder of the pulse, panel (e), and the full time $k_x > 0$ LZS interference.

however, provides a wealth of additional information, as we now describe.

By comparing rows (g)–(i) and (m)–(o) we observe almost identical residual coherent current, and yet a very different momentum space LZS excitation as revealed by the EMD. In particular, in row (m)–(o) we observe a subdominant $k_x < 0$ charge excitation absent in row (g)–(i) and reflecting multiple passes of the avoided crossing due to the side peaks of the former pulse [see panel (i)]. The presence of the main and side peaks in the pulse structure allows for multiple pass **k**-space trajectories which, due to the pulse envelope, consist of a series of passes of the avoided crossing from trajectories of different length in momentum space. This yields both asymmetric occupation and more complex interference patterns. Further enhancement of these side peaks [see row (s)–(u) of Fig. 1 for which the CEP is again $\phi = +\pi/2$] results in well developed interference fringes for both positive and negative k_x, quite different to the right-hand side only momentum space occupation seen for the lower frequency $\phi = +\pi/2$ pulse shown in panels (g)–(i). The EMD thus represents a much more sensitive probe of the LZS effect, able to unveil subtitles of the interference physics lost in the residual current.

A striking example of this richness of information provided by EMD versus the residual current can be found in row (p)–(r). Here it can be seen that widespread excitation occurs throughout the BZ driven by an intense pulse, the **A**-field of which drives trajectories right across the BZ (indicated by the lines in the $N_{\rm ex}$/EMD panels). A very complex and asymmetric LZS interference pattern results from this intense excitation; however, the widespread occupation of momentum space drives an overall cancellation of current carrying states and a vanishingly small residual current.

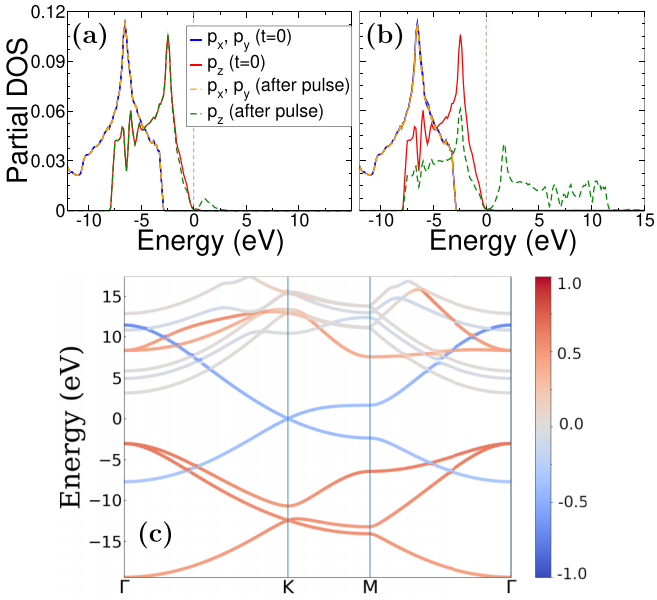

FIG. 3. Time-dependent partial density of states (PDOS) projected onto the $l = 1$ spherical harmonics. Here the PDOS (in states/atom/eV) is shown both at $t = 0$ before the pulse, and at the end of the simulation after the pulse has been applied. The pump pulse for panels (a) and (b) is polarized in the x direction, with intensities 10^{12} W/cm^2 and 10^{14} W/cm^2, respectively. As can be seen, even for almost complete excitation of the π band in which charge is excited from the π-band minima up to the π^*-band maxima, there is no excitation into states of p_x or p_y character. (c) Band structure of graphene showing the π and σ band character. Negative and positive numbers indicate dominance by π and σ character, respectively.

Experimentally, the short time coherent current ultimately generates heating and a diffusive residual current. This can therefore not provide a real time probe of the development of LZS physics. Transient EMD, on the other hand, potentially provides a real time probe of the ultrashort time evolution of LZS interference patterns in momentum space. In Fig. 2 we show the transient EMD evaluated before, during, and after a pump pulse inducing both a coherent current and LZS interference. One can observe an early time excitation due to pulse side peaks, panels (b) and (c), followed by a dramatic excitation in momentum space at the maximum of the main peak, panel (d). Only after this peak has passed do the final interference fringes develop [panels (e) and (f)].

Dominance of the π manifold in electron dynamics. The results for the momentum resolved conduction band occupation shown in the previous sections, correspond very closely to results obtained on the basis of model π-band only tight-binding Hamiltonians. This raises the question of whether this is due simply to the relatively low energies of the excited charge (in Figs. 1 and 2 the excited charge resides predominantly at the K point and the K-M-K line) or whether, for a more general reason, the π band will always dominate ultrafast laser induced electron dynamics in graphene. To explore this, in Fig. 3 we display the partial density of states calculated before and after the laser pulse. As can be seen in Fig. 3(a), for the pulse of intensity 10^{12} W/cm^2, the partial density of states (DOS) after the pulse shows conduction band occupation only up to 2.5 eV. At these energies [see Fig. 3(c)], only the π band is available for excited charge. Remarkably, when we consider a very strong pulse of intensity 10^{14} W/cm^2 the excited electrons are again only of p_z character [Fig. 3(b)], despite the fact that the laser pulse is sufficiently strong to excite charge from the minima of the π manifold up to the maxima of the π^* manifold. As may be noted from the band structure [Fig. 3(c)], within this energy range exist many other bands that would, in principle, be expected to be involved in the electron dynamics at such high energies. Examination of the relevant dipole matrix elements reveals that transitions from π to σ^* and π^* to σ are negligible for laser pulses with in-plane polarization. Thus even in the highly nonperturbative regime transitions from the ground state to the σ^* manifold will be strongly suppressed. It might be argued that the partial DOS, a projection within (touching) muffin tins, does not account for excitation to delocalized bands of high l character. Comparison of the interstitial density of states before and after the pulse shows that there is indeed an increase in interstitial charge at around 9 eV, possibly indicating transitions from the π^* manifold to delocalized bands (note the intersections between π^* and high l character bands on the M-Γ line); however, this is a rather small effect. It would thus appear that the model π-band only tight-binding Hamiltonians provide an excellent description of the electron dynamics even for very intense laser pulses.

To summarize we have investigated *ab initio* the laser induced electron dynamics in monolayer graphene. This system provides a canonical example of a material for which Landau-Zener-Stückelberg interferometry can be explored, and we have shown that direct visualization of the interference fringes in momentum space is possible via the transient EMD, establishing transient EMD as an excellent experimental tool for exploring LZS interference in 2D materials. Examination of the excited state partial density of states reveals that the π-band manifold decisively dominates ultrafast laser induced dynamics in graphene, justifying the deployment of the popular Hückel tight-binding model. Whether this remains true for the complex few layer graphene systems, for which such an approach is the only one that can reasonably be envisioned, remains an open question.

Acknowledgments. Q.Z.L. would like to thank DFG for funding through TRR227 (Project A04). S.S. would like to thank DFG for funding through SH498/4-1 and P.E. acknowledges funding from DFG Eigene Stelle Project 2059421. The authors acknowledge the North-German Supercomputing Alliance (HLRN) for providing HPC resources that have contributed to the research results reported in this Letter.

[1] A. Schiffrin, T. Paasch-Colberg, N. Karpowicz, V. Apalkov, D. Gerster, S. Mühlbrandt, M. Korbman, J. Reichert, M. Schultze, S. Holzner *et al.*, Optical-field-induced current in dielectrics, Nature (London) **493**, 70 (2013).

[2] C. Heide, T. Higuchi, H. B. Weber, and P. Hommelhoff, Coherent Electron Trajectory Control in Graphene, Phys. Rev. Lett. **121**, 207401 (2018).

[3] T. Higuchi, C. Heide, K. Ullmann, H. B. Weber, and P. Hommelhoff, Light-field-driven currents in graphene, Nature (London) **550**, 224 (2017).

[4] J. K. Dewhurst, P. Elliott, S. Shallcross, E. K. U. Gross, and S. Sharma, Laser-induced intersite spin transfer, Nano Lett. **18**, 1842 (2018).

[5] F. Siegrist, J. A. Gessner, M. Ossiander, C. Denker, Y. P. Chang, M. C. Schröder, A. Guggenmos, Y. Cui, J. Walowski, U. Martens *et al.*, Light-wave dynamic control of magnetism, Nature (London) **571**, 240 (2019).

[6] K. F. Mak, K. He, J. Shan, and T. F. Heinz, Control of valley polarization in monolayer MoS_2 by optical helicity, Nat. Nanotechnol. **7**, 494 (2012).

[7] H. Zeng, J. Dai, W. Yao, D. Xiao, and X. Cui, Valley polarization in MoS_2 monolayers by optical pumping, Nat. Nanotechnol. **7**, 490 (2012).

[8] S. N. Shevchenko, S. Ashhab, and F. Nori, Landau-Zener-Stückelberg interferometry, Phys. Rep. **492**, 1 (2010).

[9] Ya. I. Rodionov, K. I. Kugel, and F. Nori, Floquet spectrum and driven conductance in Dirac materials: Effects of Landau-Zener-Stückelberg-Majorana interferometry, Phys. Rev. B **94**, 195108 (2016).

[10] H. Ribeiro, J. R. Petta, and G. Burkard, Interplay of charge and spin coherence in Landau-Zener-Stückelberg-Majorana interferometry, Phys. Rev. B **87**, 235318 (2013).

[11] J. Stehlik, Y. Dovzhenko, J. R. Petta, J. R. Johansson, F. Nori, H. Lu, and A. C. Gossard, Landau-Zener-Stückelberg interferometry of a single electron charge qubit, Phys. Rev. B **86**, 121303(R) (2012).

[12] F. Forster, G. Petersen, S. Manus, P. Hänggi, D. Schuh, W. Wegscheider, S. Kohler, and S. Ludwig, Characterization of Qubit Dephasing by Landau-Zener-Stückelberg-Majorana Interferometry, Phys. Rev. Lett. **112**, 116803 (2014).

[13] E. Dupont-Ferrier, B. Roche, B. Voisin, X. Jehl, R. Wacquez, M. Vinet, M. Sanquer, and S. De Franceschi, Coherent Coupling of Two Dopants in a Silicon Nanowire Probed by Landau-Zener-Stückelberg Interferometry, Phys. Rev. Lett. **110**, 136802 (2013).

[14] X. Mi, S. Kohler, and J. R. Petta, Landau-Zener interferometry of valley-orbit states in Si/SiGe double quantum dots, Phys. Rev. B **98**, 161404(R) (2018).

[15] K. L. Ishikawa, Electronic response of graphene to an ultrashort intense terahertz radiation pulse, New J. Phys. **15**, 055021 (2013).

[16] A. C. Dias, F. Qu, D. L. Azevedo, and J. Fu, Band structure of monolayer transition-metal dichalcogenides and topological properties of their nanoribbons: Next-nearest-neighbor hopping, Phys. Rev. B **98**, 075202 (2018).

[17] K. Cho, J. Yang, and Y. Lu, Phosphorene: An emerging 2D material, J. Mater. Res. **32**, 2839 (2017).

[18] F. Nematollahi, V. Apalkov, and M. I. Stockman, Phosphorene in ultrafast laser field, Phys. Rev. B **97**, 035407 (2018).

[19] J. C. Garcia, D. B. de Lima, L. V. C. Assali, and J. F. Justo, Group IV graphene- and graphane-like nanosheets, J. Phys. Chem. C **115**, 13242 (2011).

[20] Y. Xu, B. Yan, H.-J. Zhang, J. Wang, G. Xu, P. Tang, W. Duan, and S.-C. Zhang, Large-Gap Quantum Spin Hall Insulators in Tin Films, Phys. Rev. Lett. **111**, 136804 (2013).

[21] H. K. Kelardeh, V. Apalkov, and M. I. Stockman, Graphene in ultrafast and superstrong laser fields, Phys. Rev. B **91**, 045439 (2015).

[22] H. K. Kelardeh, V. Apalkov, and M. I. Stockman, Attosecond strong-field interferometry in graphene: Chirality, singularity, and Berry phase, Phys. Rev. B **93**, 155434 (2016).

[23] D. Ernsting, D. Billington, T. D. Haynes, T. E. Millichamp, J. W. Taylor, J. A. Duffy, S. R. Giblin, J. K. Dewhurst, and S. B. Dugdale, Calculating electron momentum densities and Compton profiles using the linear tetrahedron method, J. Phys.: Condens. Matter **26**, 495501 (2014).

[24] Y. Sakurai, Y. Tanaka, A. Bansil, S. Kaprzyk, A. T. Stewart, Y. Nagashima, T. Hyodo, S. Nanao, H. Kawata, and N. Shiotani, High-Resolution Compton Scattering Study of Li: Asphericity of the Fermi Surface and Electron Correlation Effects, Phys. Rev. Lett. **74**, 2252 (1995).

[25] L. Dobrzyński and A. Holas, Reconstruction of the electron momentum density distribution by the maximum entropy method, Nucl. Instrum. Methods Phys. Res. Sect. A **383**, 589 (1996).

[26] W. Schülke, G. Stutz, F. Wohlert, and A. Kaprolat, Electron momentum-space densities of Li metal: A high-resolution Compton-scattering study, Phys. Rev. B **54**, 14381 (1996).

[27] G. Kontrym-Sznajd, M. Samsel-Czekała, S. Huotari, K. Hämäläinen, and S. Manninen, Fermi-surface mapping from Compton profiles: Application to beryllium, Phys. Rev. B **68**, 155106 (2003).

[28] N. Hiraoka, T. Buslaps, V. Honkimäki, J. Ahmad, and H. Uwe, Fermi surface nesting in $Ba_{1-x}K_xBiO_3$ observed by Compton scattering: Three-dimensional momentum density reconstruction study, Phys. Rev. B **75**, 121101(R) (2007).

[29] N. Hiraoka and T. Nomura, Electron momentum densities near Dirac cones: Anisotropic umklapp scattering and momentum broadening, Sci. Rep. **7**, 565 (2017).

[30] F. F. Kurp, T. Tschentscher, H. Schulte-Schrepping, J. R. Schneider, and F. Bell, 3D-electron momentum density of graphite, Europhys. Lett. **35**, 61 (1996).

[31] H. K. Kelardeh, V. Apalkov, and M. I. Stockman, Wannier-Stark states of graphene in strong electric field, Phys. Rev. B **90**, 085313 (2014).

[32] F. Fillion-Gourdeau, D. Gagnon, C. Lefebvre, and S. MacLean, Time-domain quantum interference in graphene, Phys. Rev. B **94**, 125423 (2016).

[33] C. Lefebvre, D. Gagnon, F. Fillion-Gourdeau, and S. MacLean, Carrier-envelope phase effects in graphene, J. Opt. Soc. Am. B **35**, 958 (2018).

[34] D. Gagnon, J. Dumont, F. Fillion-Gourdeau, and S. MacLean, Pulse shaping in the terahertz frequency range for the control of photo-excited carriers in graphene, J. Opt. Soc. Am. B **35**, 3021 (2018).

[35] P. Elliott, T. Müller, J. K. Dewhurst, S. Sharma, and E. K. U. Gross, Ultrafast laser induced local magnetization dynamics in Heusler compounds, Sci. Rep. **6**, 38911 (2016).

[36] E. Runge and E. K. U. Gross, Density-Functional Theory for Time-Dependent Systems, Phys. Rev. Lett. **52**, 997 (1984).

[37] C. A. Ullrich, *Time-Dependent Density-Functional Theory Concepts and Applications* (Oxford University Press, Oxford, New York, 2011).

[38] M. A. L. Marques, N. T. Maitra, F. Nogueira, E. K. U. Gross, and A. Rubio, *Fundamentals of Time-Dependent Functional Theory* (Springer-Verlag, Berlin/Heidelberg, 2012).

[39] D. J. Singh, *Planewaves Pseudopotentials and the LAPW Method* (Kluwer Academic, Boston, 1994).

[40] J. K. Dewhurst *et al.*, elk.sourceforge.net/ (2020).

[41] K. Krieger, J. K. Dewhurst, P. Elliott, S. Sharma, and E. K. U. Gross, Laser-induced demagnetization at ultrashort time scales: Predictions of TDDFT, J. Chem. Theory Comput. **11**, 4870 (2015).

[42] J. K. Dewhurst, K. Krieger, S. Sharma, and E. K. U. Gross, An efficient algorithm for time propagation as applied to linearized augmented plane wave method, Comput. Phys. Commun. **209**, 92 (2015).

[43] A. K. Rajam, P. Hessler, C. Gaun, and N. T. Maitra, Phase-space explorations in time-dependent density functional theory, J. Mol. Struct.: THEOCHEM **914**, 30 (2009).

[44] P. Elliott and N. T. Maitra, Electron correlation via frozen Gaussian dynamics, J. Chem. Phys. **135**, 104110 (2011).